Vacuum 146 (2017) 35–43

Contents lists available at ScienceDirect

Vacuum

journal homepage: www.elsevier.com/locate/vacuum

Hot workability and constitutive model of the Cu-Zr-Nd alloy

Yi Zhang [a, b, *], Huili Sun [a, b, **], Alex A. Volinsky [c], Baohong Tian [a, b], Kexing Song [a, b], Bingjie Wang [a, b], Yong Liu [a, b]

[a] School of Materials Science and Engineering, Henan University of Science and Technology, Luoyang 471003, China
[b] Collaborative Innovation Center of Nonferrous Metals, Henan Province, Luoyang 471003, China
[c] Department of Mechanical Engineering, University of South Florida, Tampa 33620, USA

ARTICLE INFO

Article history:
Received 26 July 2017
Received in revised form
5 September 2017
Accepted 8 September 2017
Available online 12 September 2017

Keywords:
Hot deformation
Cu-Zr-Nd alloy
Processing map
Constitutive equation

ABSTRACT

Hot deformation behavior of the Cu-Zr-Nd alloy was studied by using compressive tests in the temperature range of 550–900 °C and the strain rate range of 0.001–10 s^{-1} on the Gleeble-1500D thermo-mechanical simulator. The Cu-Zr-Nd alloy flow stress increased at higher strain rate and lower temperature. Based on the processing maps and microstructure, the optimal processing parameters for the Cu-Zr-Nd alloy are determined as 750-870 °C and 0.001–0.03 s^{-1}. The addition of Nd can promote the dynamic recrystallization. A new constitutive model, which compensates for the strain rate, is established according to the Arrhenius-type equation. The Zener-Hollomon parameter was also modified to compensate for the strain rate. The flow stress predicted by the constitutive equation is consistent with the experimental flow stress.

1. Introduction

Copper-based alloys have excellent electrical conductivity, fine thermal conductivity, good corrosion resistance and high strength. They are extensively used as aerial conductors in electronics engineering and in automobiles [1,2]. In particular, a great number of scholars agree that copper alloys are ideal materials for integrated circuit (IC) lead frame [3], railway contacts [4] and first wall of the reactor vacuum vessels [5]. With the rapid development of industrial technology, higher performance is required of copper alloys. Metallic elements can be added in the process of the alloy preparation to improve physical and mechanical properties. For example, Zhou et al. [6] reported that the addition of Cr can increase the strength of Cu alloys by pinning dislocations at the precipitates. Some researches [7,8] showed that the addition of Zr has little effect on Cu alloys due to low 0.15% solid solubility of Zr in Cu at 1239 K (966 °C), which is rapidly reduced with temperature decrease. What's more, the recrystallization temperature of the copper alloy is increased significantly due to the addition of Zr. Cu-Zr alloy has good aging precipitation strengthening effect. Many researchers show that small amounts of Zr can improve the strength of the alloy significantly, but have a little effect on the alloy conductivity [9,10]. After heat treatment of the Cu-7wt.%Ag-0.05 wt%Zr alloy, Gaganov et al. obtained a promising conductor with high strength. The results showed that the tensile strength is 1360 MPa, while the tensile strength of Cu-7wt.%Ag alloy is 1220 MPa, which is about 140 MPa lower than the above-mentioned alloy. However, these studies dealt with the aging behavior of the Cu-Zr alloy, and little analysis of the hot deformation behavior of the Cu-Zr alloy was performed. Rare earth elements (RE) have been described as “vitamins” for metals [11]. A lot of researches indicate that RE can purify the alloy matrix and the grain boundaries, ameliorating the conductivity and softening temperature of the alloy, while improving its strength [12–14]. Thus, the trace Re addition can improve the chemical and mechanical properties significantly. In our previous study, Cu-Cr-Zr-Nd alloy was investigated, and it was found that the addition of Nd can improve dynamic recrystallization (DRX) during hot deformation by refining the grains of the Cu-Cr-Zr alloy [15]. In this study, a small amount of Nd was added into the Cu-Zr alloy to research the effect of Nd on its properties.

The Cu-Cr-Zr alloy has been used in the International Thermonuclear Experimental Reactor (ITER) as the first wall of the reactor vacuum vessel. In order to improve the radiation resistance, many processing methods were used, such as equal channel

* Corresponding author. School of Materials Science and Engineering, Henan University of Science and Technology, Luoyang 471003, China.
** Corresponding author. School of Materials Science and Engineering, Henan University of Science and Technology, Luoyang 471003, China.
E-mail addresses: zhshgu436@163.com (Y. Zhang), shllt0909@126.com (H. Sun).

http://dx.doi.org/10.1016/j.vacuum.2017.09.017
0042-207X/

angular pressing, rolling and extrusion [16]. For the Cu-Cr-Zr alloy, the processing methods are also very important to improve its properties. In all of the methods, an accurate constitutive equation can represent the relationships between the strain rate, temperature, and the flow stress. Thus, more attention has been paid to developing an accurate constitutive equation [17]. However, the effect of strain in the constitutive equation has been ignored. The proper constitutive relationship for the Cu-0.2%Zr-0.15%Nd alloy need to be further studied to represent the effects of strain compensation.

In this paper, hot deformation behavior of the Cu-0.2%Zr-0.15% Nd alloy was investigated under different deformation conditions by hot compression tests on the Gleeble-1500 simulator. Through the test data analysis, the effects of temperature and strain rate on flow stress were studied. An accurate constitutive equation to predict the flow stress for the studied alloy has been obtained. Furthermore, based on the experimental results, the hot processing maps based on the dynamic material model (DMM) were built, and the optimal processing parameters for the Cu-Zr-Nd alloy were determined.

2. Experimental details

The deformable material used in this study was Cu-Zr-Nd alloy. The chemical composition is given in Table 1. The alloy was cast at 1200-1250 °C in a vacuum induction furnace. During the whole process, argon was used as a protective gas. Before the experiment, the ingot was homogenized by solution heat treatment at 900 °C for 1 h and water quenched. The microstructure after the heat treatment is shown in Fig. 1. Then the specimens with Φ8 mm × 12 mm dimensions were machined.

The hot compression tests were conducted directly on the Gleeble-1500D thermo-mechanical simulator with the total deformation of 55%. The deformation temperature was 550–900 °C with the strain rate of 0.001–1 s^{-1}. The specimens were heated to 900 °C at 20 °C/s heating rate, and then held for 6 min to achieve uniform temperature distribution before compression testing. In order to improve the accuracy, graphite tantalum sheets were placed at the ends of the cylinder sample to reduce friction. As soon as the compression tests were completed, the specimens were immediately water cooled to retain the hot deformation microstructure, which was examined by the OLYMPUS PMG3 optical microscope. For optical microscopy, the specimens were mechanically polished and etched with a solution containing $HCl + C_2H_5OH + FeCl_3$.

3. Results and discussion

3.1. Flow stress behavior analysis

The true strain-stress curves of the Cu-Zr-Nd alloy under different deformation conditions are shown in Fig. 1. It can be seen that the deformation temperature and initial strain rate really affect the flow stress during the hot deformation. It is well known that the hot deformation is a competing process between the work hardening and the dynamic softening. The flow stress increases with temperature decrease, and increases with higher strain rate. In its infancy, the flow stress increases with the strain due to work hardening. It can be generalized into two mechanisms according to its subsequent variation characteristics [18,19]. One kind is dynamic recovery (DRV), as shown at the deformation temperature of 650 °C in Fig. 1(a) and (b). In the final stage, the work hardening and dynamic softening reach a balance and the flow stress remains constant. This generally occurs at lower temperature. Another kind is dynamic recrystallization (DRX). The flow curves reach to a peak value first, and then decrease until a relatively steady constant value is achieved in the end. This can be seen at the deformation temperatures of 850 °C and 900 °C in Fig. 1.

Table 1
Chemical composition of the studied alloy in wt.%.

Element	Zr	Nd	Cu
Wt.%	0.2	0.15	Bal.

3.2. Microstructure evolution

3.2.1. Hot workability and optical micrographs of the Cu-Zr-Nd alloy

The processing maps in this paper are plotted based on the dynamic material model [20], which takes the flow stress, hot deformation temperature, strain and strain rate into account. The principles for producing the processing maps have been clearly described by Prasad [21].

During hot deformation, the input energy (P) can be roughly divided into two major parts: some of the energy (G) is used for plastic deformation, while another fraction is emitted as microstructure evolution (J). The corresponding relationship between them can be described as:

$$P = G + J \tag{1}$$

The energy for the microstructure evolution is defined as η, which can be expressed as:

$$\eta = \frac{J}{J_{max}} = \frac{2m}{m+1} \times 100\% \tag{2}$$

Where m is the strain rate sensitivity index, defined as:

$$m = \frac{\dot{\varepsilon} d\sigma}{\sigma d\dot{\varepsilon}} = \left[\frac{\partial(\ln \sigma)}{\partial(\ln \dot{\varepsilon})}\right]_{\varepsilon,T} \cong \frac{d \ln \sigma}{d \ln \dot{\varepsilon}} \tag{3}$$

According to the dynamic material model, the instability criterion can be described as:

$$\xi(\dot{\varepsilon}) = \frac{\partial \ln[m/(m+1)]}{\partial \ln \dot{\varepsilon}} + m < 0 \tag{4}$$

Fig. 2 shows the processing maps of the Cu-Zr-Nd alloy under different strain. It can be clearly seen that there are two different parts of the maps – a part of flow instabilities, which is shadowed, and a part of flow stability where ideal microstructure can be observed.

Comparing the four processing maps, the instability domains mainly exist at high strain rates. At high strain rate, shear bands are found. Typical optical microstructure is shown in Fig. 4 (b) for the alloy deformed at 650 °C and 10 s^{-1}. The average grain size is about 70 μm. However, this may be primarily because the time is too short for microstructure evolution. Many researches [15] show that the optimal processing areas are located at stable regions with high power efficiency. However, the analysis of the power efficiency was comparatively rare. In this paper, a 3D power efficiency map for the Cu-Zr-Nd alloy at different strain is shown in Fig. 3. In Fig. 3, a lower value of η was found at lower strain of 0.1 and 0.2. At higher strain, the change of η is comparatively uniform. This may be because elastic deformation is the major deformation mechanism at the early stages of compression deformation [22]. Generally, the power efficiency has the same varying tendency under different strain conditions; it changes with the temperature and the strain rate. The value of the power efficiency increases dramatically at higher temperature and lower strain rate. The higher the strain, the larger

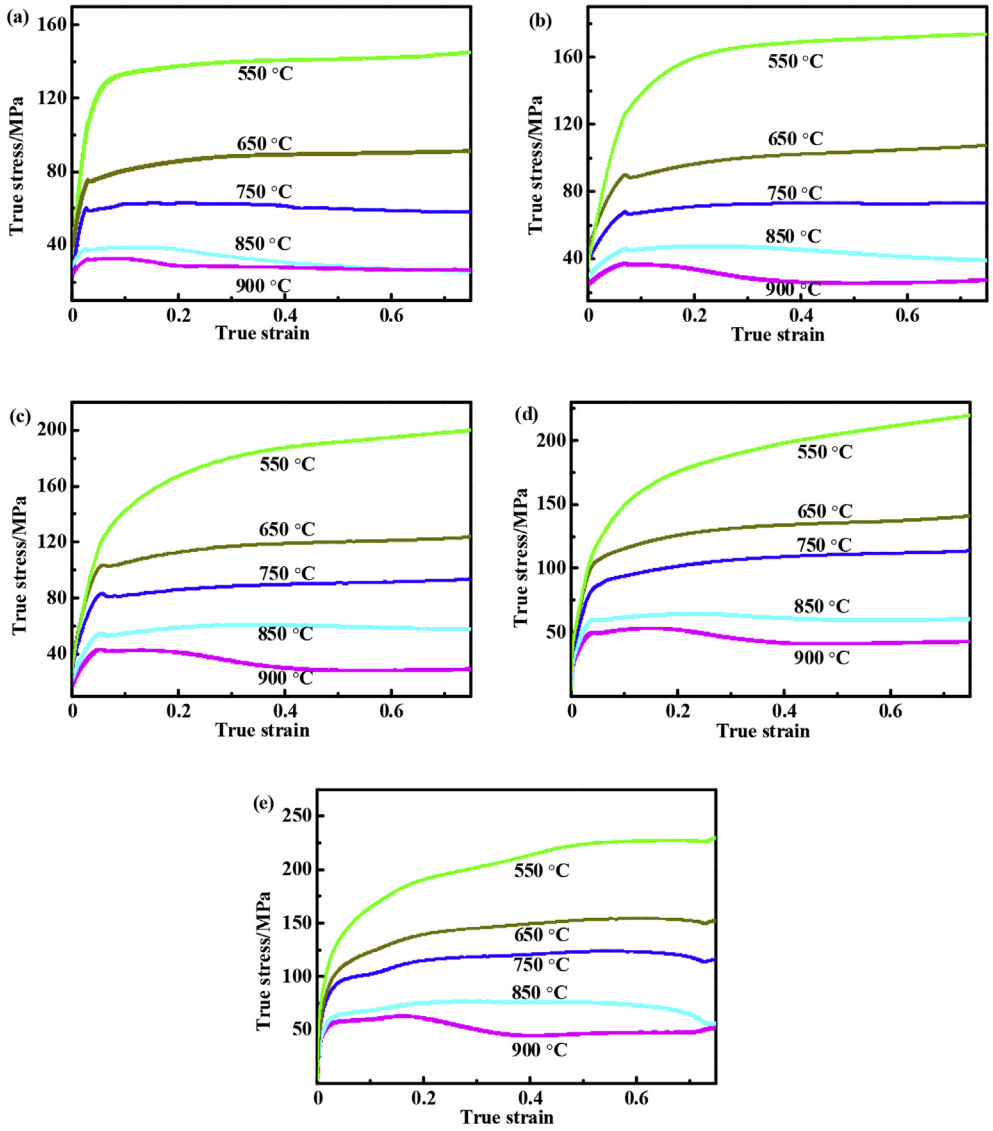

Fig. 1. True stress-strain curves of the Cu-Zr-Nd alloy under different deformation conditions: (a) 0.001 s^{-1}; (b) 0.01 s^{-1}; (c) 0.1 s^{-1}; (d) 1 s^{-1}; (e) 10 s^{-1}.

the average power efficiency value is. High value of power dissipation means that more energy was available for microstructure evolution. However, high power efficiency does not automatically mean good workability. Deformation twins or micro cracks may cause high power efficiency [23]. Thus, proper microstructure is necessary to determine the optimal working conditions. Fig. 4(b) illustrates microstructure obtained at low strain rate and temperature (650 °C and 0.001 s^{-1}), where many typical microstructure necklaces can be clearly observed. Many DRX grains can be clearly observed in Fig. 4(c) with temperature increase, with an average grain size of 39 μm. The corresponding power efficiency ranges from 26% to 36%. This means that the alloys under these conditions exhibit good processing performance. The value of the power efficiency decreases if the hot deformation temperature is too high. The same results are obtained by Cheng [24]. Fig. 4(d) shows the microstructure at 900 °C and 0.1 s^{-1}, corresponding to the domain marked with M in Fig. 3. Many larger grains are present in the microstructure. The reason for that is the smaller grains along with the more boundaries can offer more nucleation sites for the dynamic recrystallization. Dehghan-Manshadi et al. [25] draw the conclusion that the dynamic recrystallization starts more rapidly with the smaller grains, which can offer higher kinetics.

Based on the above analyses, the optimal processing parameters for the Cu-Zr-Nd alloy are determined as the temperature range of 750–870 °C and the strain rate range of 0.001–0.03 s^{-1}, and the efficiency of power dissipation of 26–36%. The processing region for the Cu-Zr-Nd alloy is wider than for the Cu-Cr-Zr-Nd alloy (900-950 °C, 0.1–1 s^{-1}), which means that the hot workability of the Cu-Zr-Nd alloy is better than the Cu-Cr-Zr-Nd alloy. This may be because the addition of Cr is deleterious to the ductility of the studied alloy [26].

3.2.2. *Transmission electron micrographs of the Cu-Zr-Nd alloy*

Transmission electron micrographs (TEM) of the Cu-Zr-Nd alloy deformed at different conditions are shown in Fig. 5. According to Fig. 5 (a), deformation grains of the deformed alloy exist in a obviously flat structure. A mass of dislocations are observed, along with the dislocation walls formed through annihilation, propagation and slip. The deformation conditions in Fig. 5(a) are 650 °C and 0.001 s^{-1}. Along with the continuously increment of temperature, dynamic recrystallization occurs in the microstructure. High dislocation density and many twins are present in Fig. 5 (b) for the

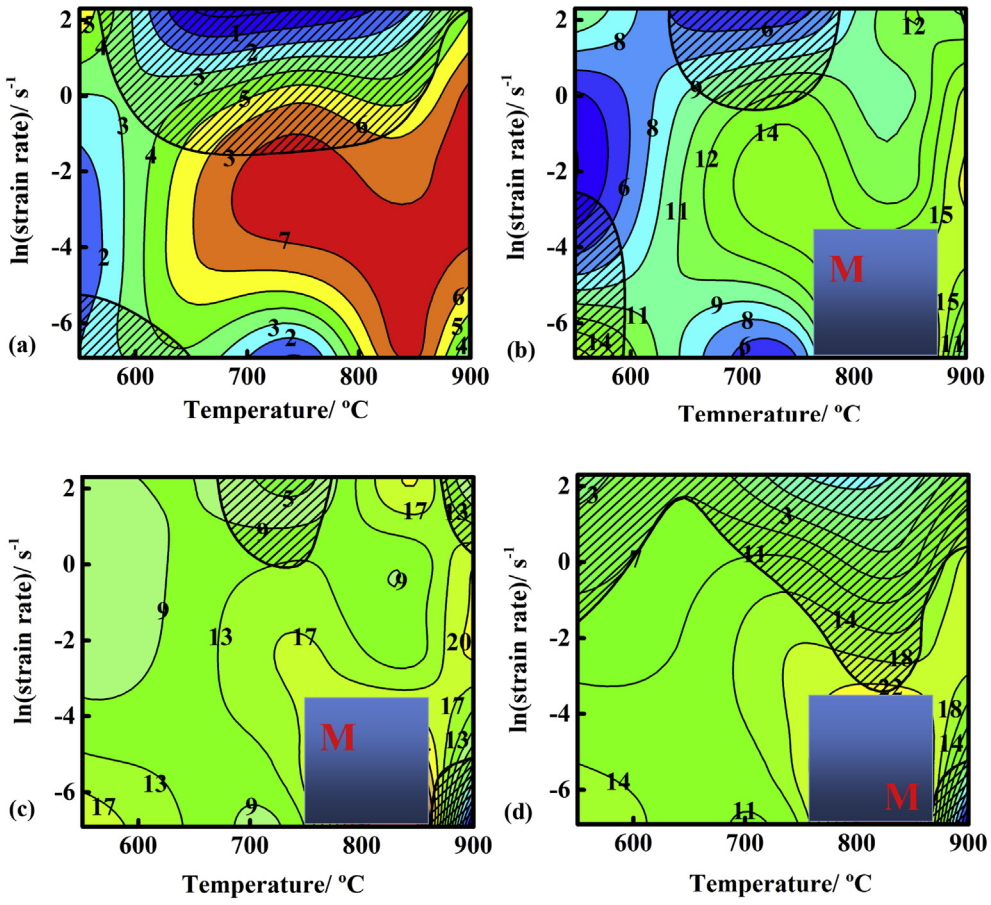

Fig. 2. Processing maps of the Cu-Zr-Nd alloy under different strain: (a) ε = 0.1; (b) ε = 0.2; (c) ε = 0.5; (d) ε = 0.7.

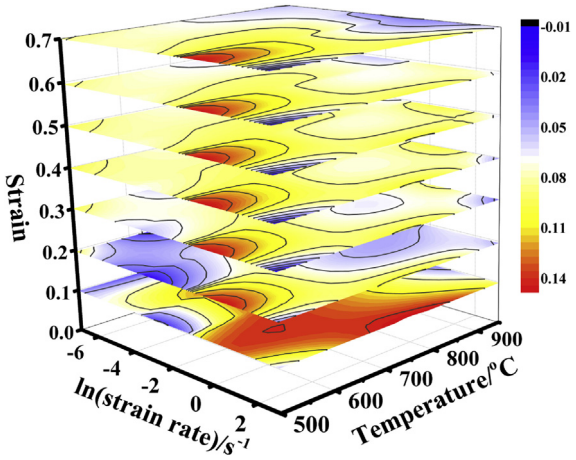

Fig. 3. Power efficiency of the Cu-Zr-Nd alloy.

alloy deformed at 850 °C and 10 s^{-1}. With the strain rate decreasing to 1 s^{-1}, there are a lot of dynamic recrystallization grains in Fig. 5(c). This means that DRX occurred at these conditions. According to Fig. 5(d), at 850 °C and 0.01 s^{-1}, the big grains have swallowed up the small grains, and the angle boundaries of the grain expand from small to large.

3.3. Establishing Arrhenius-type constitutive equations

There are many constitutive models to interpret the plastic deformation behavior and to predict the flow stress during hot deformation [27,28]. Arrhenius type equation is an accurate approach to describe the relationships between the flow stress, strain rate and deformation temperature. These can be described with the following equations [29,30].

$$\dot{\varepsilon} = A_1\sigma^n \exp\left(-\frac{Q}{RT}\right) \quad (\alpha\sigma < 0.8) \tag{5}$$

$$\dot{\varepsilon} = A_2 \exp(\beta\sigma)\exp\left(-\frac{Q}{RT}\right) \quad (\alpha\sigma > 1.2) \tag{6}$$

$$\dot{\varepsilon} = A[\sinh(\alpha\sigma)]^{n_1} \exp\left(-\frac{Q}{RT}\right) \quad (\text{all}) \tag{7}$$

Where, $\dot{\varepsilon}$-the strain rate, s^{-1}; σ-the flow stress, MPa; R-the universal gas constant, 8.314 J mol^{-1} K^{-1}; T-the thermodynamic temperature, K; Q-the activation energy of hot deformation, KJ mol^{-1}; A_1, A_2, A, n and n_1 are all the correlative materials constants; α is stress multiplier, defined as $\alpha = \beta/n_1$.

In the meantime, the common influence of the strain rate and high temperature on the hot deformation behavior can be represented by an exponent-type equation, which was proposed by Sellars and McTegart [31,32]. It can be adequately expressed by the Zener-Hollomon parameter (Z) [33], which is a function of temperature and stress:

$$Z = \dot{\varepsilon}\exp\left(\frac{Q}{RT}\right) = A[\sinh(\alpha\sigma)]^{n_1} \tag{8}$$

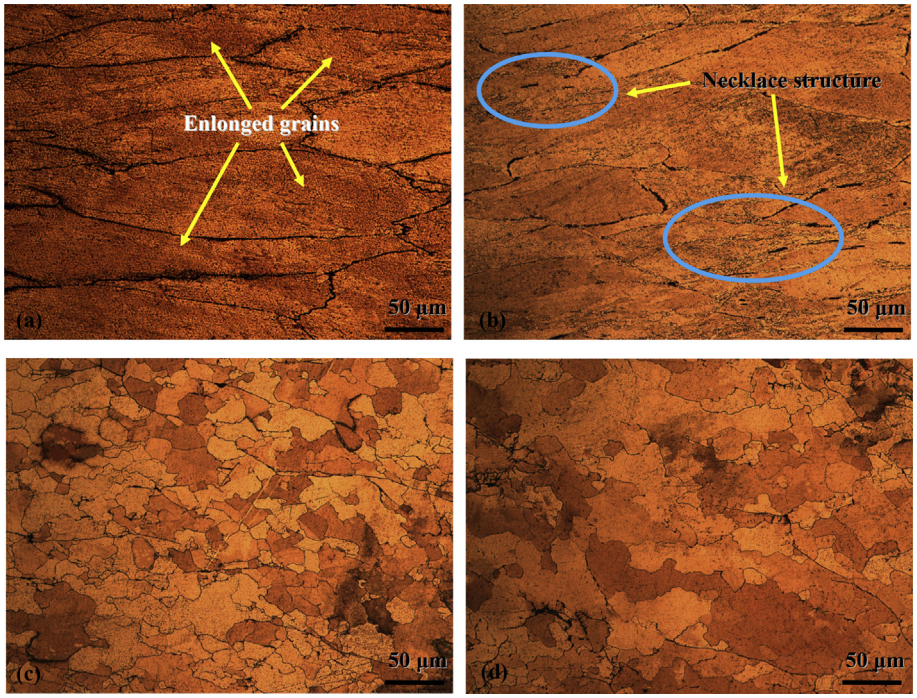

Fig. 4. Optical images of the Cu-Zr-Nd alloy microstructure deformed at: (a) 923 K (650 °C) and 10 s^{-1}; (b) 923 K (650 °C), 0.001 s^{-1}; (c) 1123 K (850 °C); 0.1 s^{-1}; (d) 1173 K (900 °C), 0.1 s^{-1}.

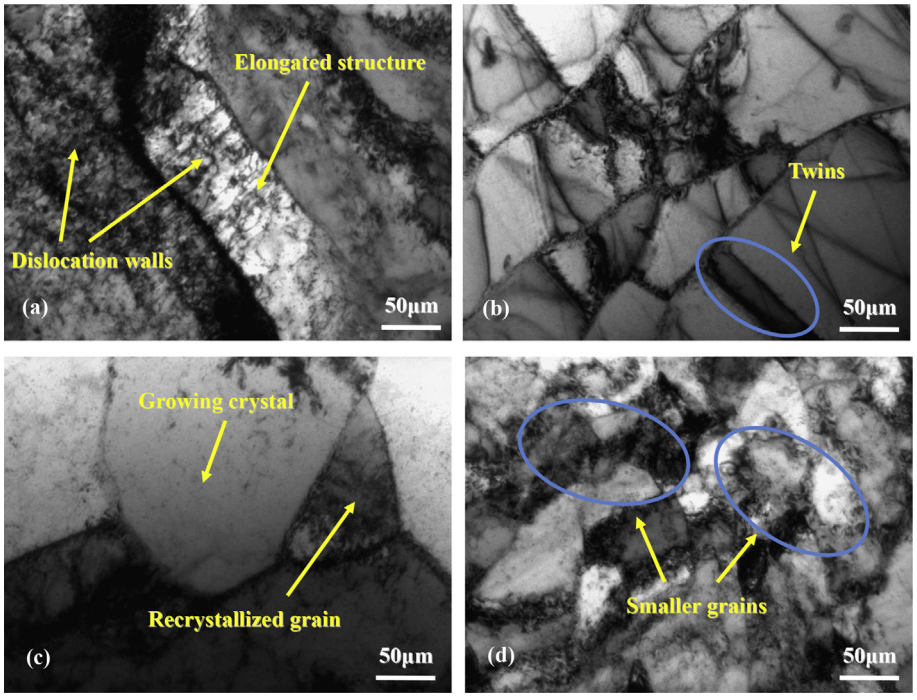

Fig. 5. TEM images of the Cu-Zr-Nd alloy deformed at: (a) 923 K (650 °C) and 0.1 s^{-1}; (b) 1123 K (850 °C), 10 s^{-1}; (c) 1123 K (850 °C); 0.01 s^{-1}; (d) 1123 K (850 °C), 1 s^{-1}.

Taking natural logarithms of the two sides of Eqs. (1), (2) and (4), yields:

$$\ln\dot{\varepsilon} = \ln A_1 - \left(\frac{Q}{RT}\right) + n \ln \sigma \tag{9}$$

$$\ln\dot{\varepsilon} = \ln A_2 - \frac{Q}{RT} + \beta\sigma \tag{10}$$

$$\ln Z = \ln A + n_1 \ln[\sinh(\alpha\sigma)] \tag{11}$$

In this paper, to calculate the material constants, we take the deformation strain of 0.1 as an example. Fig. 6(a) shows the

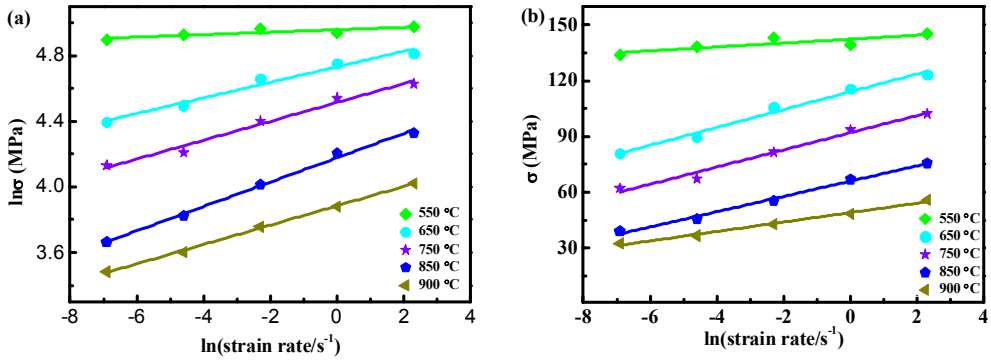

Fig. 6. Relationships between (a) lnσ and lnε; (b) σ and lnε.

relationship between ln$\dot{\varepsilon}$ and lnσ. By using a combination of Eq. (9) and Fig. 6(a), one can get the value of n, which takes the mean value among the slopes of the straight lines in Fig. 6(a). In the same respect, one can easily work out the value of β. Therefore, the mean values of $n = 20.359$ and $\beta = 0.292$ MPa^{-1} can be obtained by calculation. Subsequently, one can get the value of $\alpha = \beta/n = 0.014$ MPa^{-1}.

Fig. 7 shows scatter diagrams. The correlations between ln$\dot{\varepsilon}$ and ln[sinh($\alpha\sigma$)], T^{-1} and ln[sinh($\alpha\sigma$)] are shown in Fig. 7(a) and (b). The data were treated with the regression analysis. The results show that the function depends linearly on ln and ln[sinh($\alpha\sigma$)], T^{-1} and ln [sinh($\alpha\sigma$)]. The average of five straight slopes in Fig. 7 are S and n'. The values of s and n' are 14.5 and 4.59, respectively.

Taking the logarithm of the two sides of Eq. (7), and differentiating yields:

$$Q = R\frac{\partial \ln[\sinh(\alpha\sigma)]}{\partial(1/T)}\bigg|_{\dot{\varepsilon}}\bigg|\frac{\partial \ln\dot{\varepsilon}}{\partial \ln[\sinh(\alpha\sigma)]}\bigg|_{T} = Rn'S \tag{12}$$

The value of Q at 0.1 strain can be calculated as 553.338 kJ mol^{-1}.

The relationship between ln[sinh($\alpha\sigma$)] and ln$Z$ is shown in Fig. 8. The slope and the intercept of the fitting straight line are the value of n_1 and ln$A$, respectively. In summary, ln$A = 59.319$, $n_1 = 14.119$, and the constitutive equation for the alloy is:

$$\dot{\varepsilon} = 5.777 \times 10^{25}[\sinh(0.014\sigma)]^{14.119}\exp\left(-\frac{553338}{8.314T}\right) \tag{13}$$

3.4. Compensation for strain

Many analyses considered that the above material constants are not important and usually ignore their effects on the flow stress [34]. Through the above analysis, the solution procedure of the material constants can impact the flow stress during the hot deformation process. It is not difficult to understand that the above material constants are crucial for the whole hot deformation. Many studies have shown that the material constants are strongly affected by the strain [35,36]. In this paper, the values of material constants were computed in diverse strain range between 0.1 and 0.7 in 0.05 increments. In order to represent the influence of strain on the material constants visually, the values obtained were fitted by the 6th order polynomials, as shown in Fig. 9. The relationship can be expressed as:

$$\ln A = A_0 + A_1\varepsilon + \ldots + A_n\varepsilon \quad (n = 5, 6, 7)$$

$$n = n_0 + n_1\varepsilon + \ldots n_n\varepsilon \quad (n = 5, 6, 7)$$

$$Q = Q_0 + Q_1\varepsilon + \ldots + Q_n\varepsilon \quad (n = 5, 6, 7)$$

$$\alpha = \alpha_0 + \alpha_1\varepsilon + \ldots + \alpha_n\varepsilon \quad (n = 5, 6, 7) \tag{14}$$

The 6th order polynomial fitting results are listed in Table 2.

3.5. Verification of the developed constitutive equation

The relationship between a given strain and the materials constants is evaluated, and the flow stress can be predicted. Based on Eq. (8), the flow stress can be calculated by the following equation, which is a function of the Zener-Hollomon parameter:

$$\sigma = \frac{1}{\alpha}\ln\left\{\left(\frac{Z}{A}\right)^{1/n} + \left[\left(\frac{Z}{A}\right)^{2/n} + 1\right]^{1/2}\right\} \tag{15}$$

With the obtained materials constants, the flow stress at arbitrary experimental conditions can be predicted. Fig. 10 shows the comparison between the experimental and predicted flow stress at a given strain rate. The results show that the calculated data agree with the experimental results, indicating that the established constitutive model is fairly accurate for predicting the flow stress during hot deformation.

In order to assess the credibility of the model, the following statistical parameters were used: correlation coefficient (R), mean squared error (RMSE), and average relative error (AARE) to measure the forecasting ability. They are represented with the following equations:

$$R = \frac{\sum_{i=1}^{N}\left(\sigma_e^i - \overline{\sigma}_e\right)\left(\sigma_p^i - \overline{\sigma}_p\right)}{\sqrt{\sum_{i=1}^{N}\left(\sigma_e^i - \overline{\sigma}_e\right)^2}\sqrt{\sum_{i=1}^{N}\left(\sigma_p^i - \overline{\sigma}_p\right)^2}} \tag{16}$$

$$RMSE = \sqrt{\frac{1}{N}\sum_{i=1}^{N}\left(\sigma_e^i - \sigma_p^i\right)^2} \tag{17}$$

$$AARE(\%) = \frac{1}{N}\sum_{i=1}^{N}\left|\frac{\sigma_e^i - \sigma_p^i}{\sigma_e^i}\right| \times 100 \tag{18}$$

Where, σ_e-the experimental flow stress, MPa; σ_p-the predicted flow stress, MPa; $\overline{\sigma}_e$, $\overline{\sigma}_p$ is the average values of σ_e, σ_p, respectively. N is the number of experimental data points.

Fig. 11 shows the experimental data and the predicted flow stress. From these result, one can find the values of R = 0.983, AARE = 8.11% and RMSE = 7.49. Therefore, the values of AARE and RMSE are low, which demonstrates that the established model has

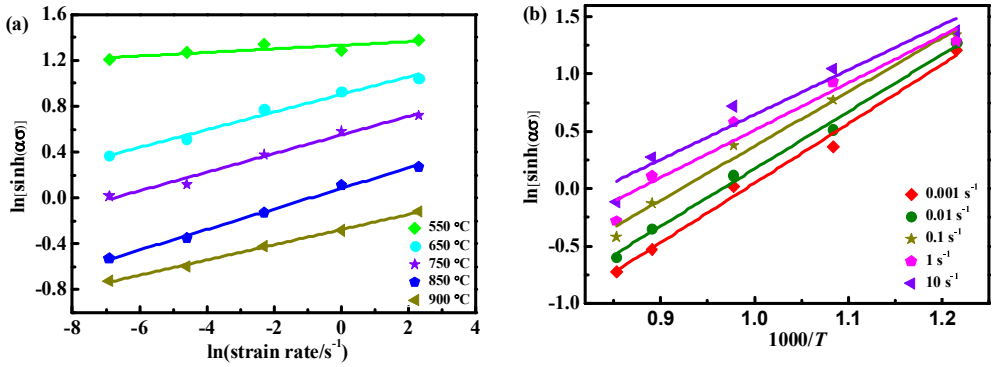

Fig. 7. Relationships between (a) lnε and ln[sinh($\alpha\sigma$)]; (b) 1/T and ln[sinh($\alpha\sigma$)].

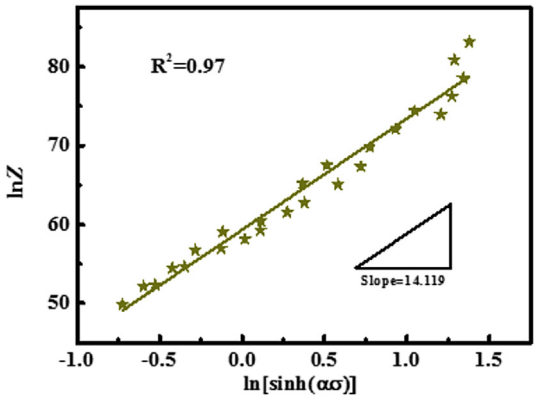

Fig. 8. Relationship between ln[sinh($\alpha\sigma$)] and lnZ.

Table 2
The 6th order polynomial fitting results.

ln$A$	n	Q	α
A_0 = 76.71	n_0 = 21.53	Q_0 = 771.41	α_0 = 0.02
A_1 = -154.90	n_1 = -106.06	Q_1 = -3041.03	α_1 = -0.11
A_2 = -786.14	n_2 = 357.26	Q_2 = 7370.96	α_2 = 0.74
A_3 = 10101.29	n_3 = -205.53	Q_3 = 29749.91	α_3 = -2.73
A_4 = -31676.35	n_4 = -1242.93	Q_4 = -154184.40	α_4 = 5.34
A_5 = 40454.28	n_5 = 2397.19	Q_5 = 228216.92	α_5 = -5.26
A_6 = -18521.92	n_6 = -1242.99	Q_6 = -112272.83	α_6 = 2.05

good predictability of the flow stress for the Cu-Zr-Nd alloy.

4. Conclusions

Higher temperature compression tests of the Cu-Zr-Nd alloy were conducted by using a thermo-mechanical simulator under different deformation conditions. The following conclusions can be

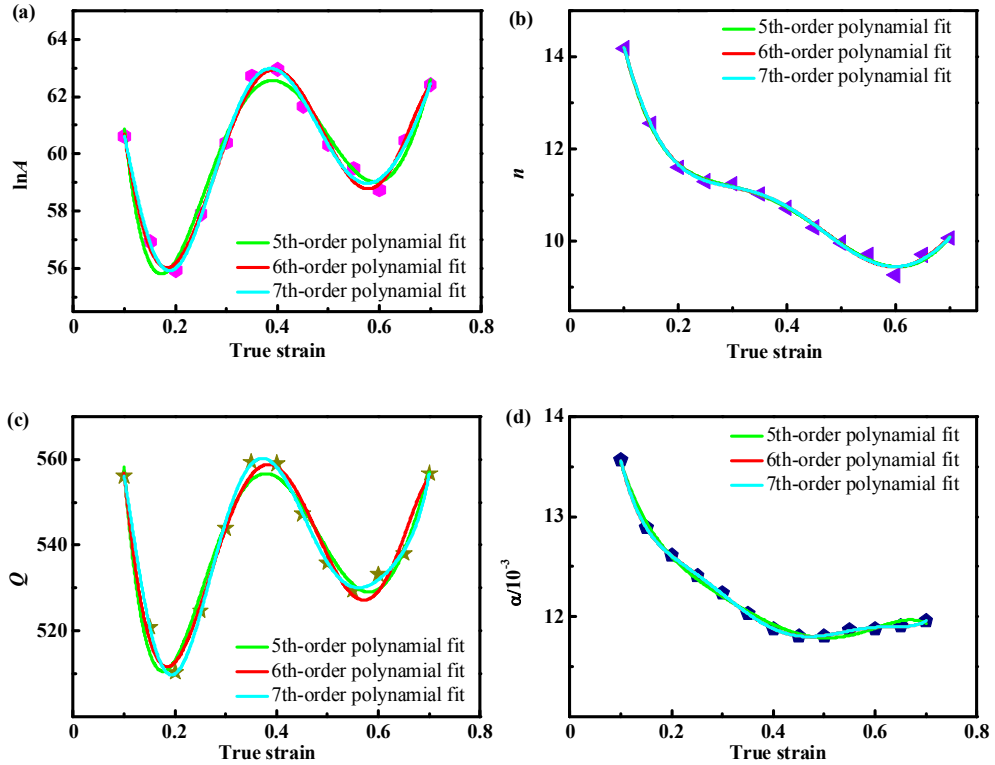

Fig. 9. Variation of (a) ε-ln$A$, (b) ε-n, (c) ε-Q and (d) ε-α with true strain.

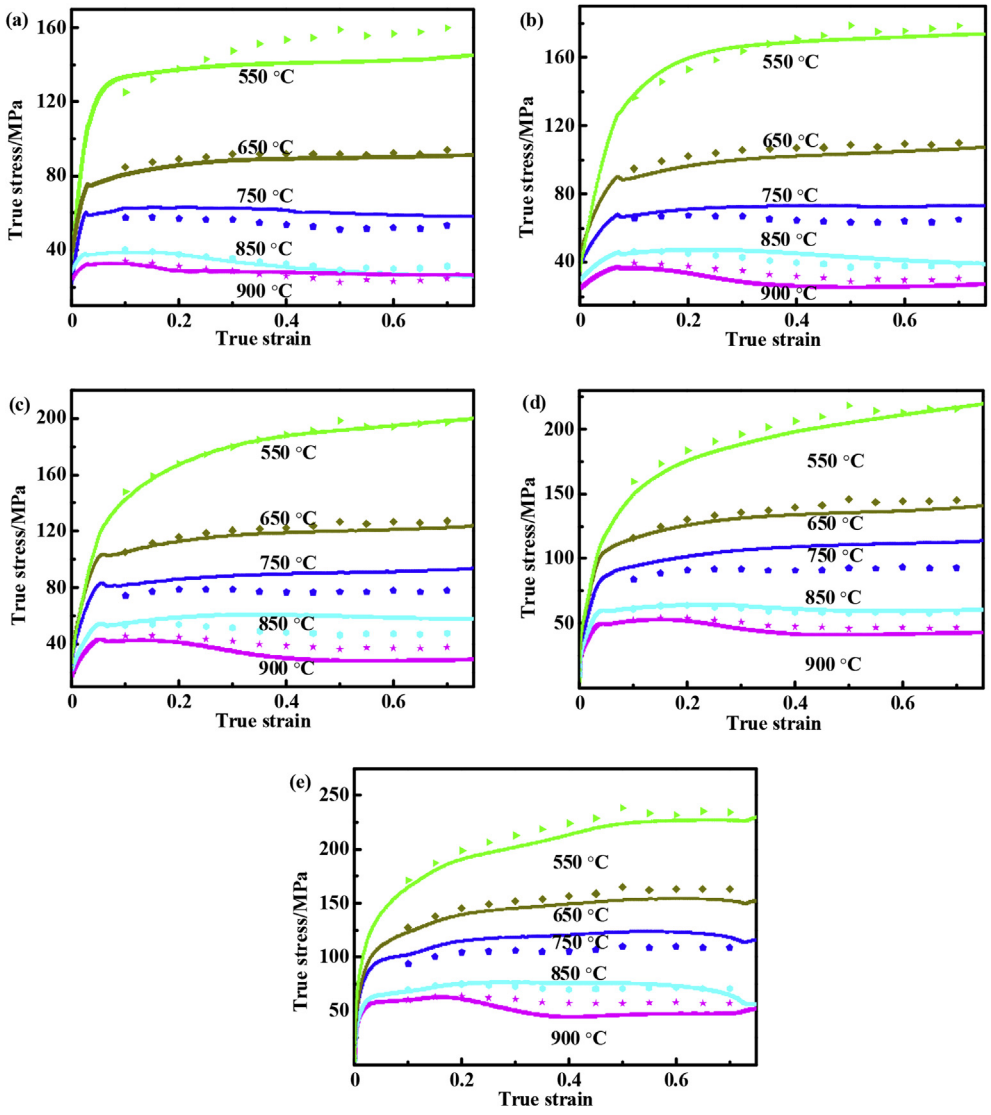

Fig. 10. Comparison between the predicted and experimental flow stress at the strain rate of: (a) 0.001 s^{-1}; (b) 0.01 s^{-1}; (c) 0.1 s^{-1}; (d) 1 s^{-1} and (d) 10 s^{-1}.

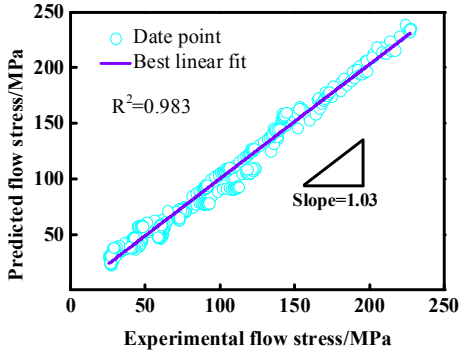

Fig. 11. Correlation between predicted and experimental flow stress values.

drawn:

(1) The flow stress of the Cu-Zr-Nd alloy is sensitive to temperature and the strain rate. It increases with the strain rate, and reduces with decreasing deformation temperature.

(2) The optimal processing parameters for the Cu-Zr-Nd alloy are determined at the temperature range of 750–870 °C and the strain rate range of 0.001–0.03 s^{-1}, with 26–36% power dissipation efficiency.

(3) The established constitutive model adequately predicts the flow stress with the corresponding values of R, AARE and RMSE of 0.983, 8.11% and 7.49, respectively. The Zener-Hollomon parameter considering the compensation for the strain rate is proposed.

Acknowledgements

This work was supported by the National Natural Science Foundation of China (51101052) and the National Science Foundation (IRES 1358088).

References

[1] Z.Q. Wang, Y.B. Zhong, G.H. Cao, C. Wang, J. Wang, W.L. Ren, Z.S. Lei, Z.M. Ren, Influence of dc electric current on the hardness of thermally aged Cu-Cr-Zr alloy, J. Alloys Comp. 479 (2009) 303–306.

[2] A.Y. Khereddine, F.H. Larbi, H. Azzeddine, T. Baudin, F. Brisset, A.L. Helbert, M.H. Mathon, M. Kawasaki, D. Bradai, T.G. Langdon, Microstructures and

textures of a Cu-Ni-Si alloy processed by high-pressure torsion, J. Alloys Comp. 574 (2013) 361–367.
[3] C.D. Xia, Y.L. Jia, W. Zhang, K. Zhang, Q.Y. Dong, G.Y. Xu, M.P. Wang, Study of deformation and aging behaviors of a hot rolled-quenched Cu-Cr-Zr-Mg-Si alloy during thermomechanical treatments, Mater. Des. 39 (2012) 404–409.
[4] Y. Zhang, Z. Chai, A.A. Volinsky, B.H. Tian, H.L. Sun, P. Liu, Y. Liu, Processing maps for the Cu-Cr-Zr-Y alloy hot deformation behavior, Mater. Sci. Eng. A 662 (2016) 320–329.
[5] V.R. Barabash, G.M. Kalinin, S.A. Fabritsiev, S.J. Zinkle, Specification of CuCrZr alloy properties after various thermo-mechanical treatments and design allowables including neutron irradiation effects, J. Nucl. Mater. 417 (2011) 904–907.
[6] J.M. Zhou, D.G. Zhu, L.T. Tang, X.S. Jiang, S. Chen, X. Peng, C.F. Hu, Microstructure and properties of powder metallurgy Cu-1%Cr-0.65%Zr alloy prepared by hot pressing, Vacuum 131 (2016) 156–163.
[7] H. Okamoto, Cu-Zr (copper-zirconium), J. Phase Equilib. Diff. 29 (2008) 204.
[8] X.H. Yang, J.T. Zou, P. Xiao, X.H. Wang, Effects of Zr addition on properties and vacuum arc characteristics of Cu-W alloy, Vacuum 106 (2014) 16–20.
[9] A. Gaganov, J. Freudenberger, E. Botcharova, L. Schultz, Effect of Zr additions on the microstructure, and the mechanical and electrical properties of Cu-7wt.%Ag alloys, Mater. Sci. Eng. A 437 (2006) 313–322.
[10] G. Kalinin, V. Barabash, A. Cardella, J. Dietz, K. Ioki, R. Matera1, R.T. Santoro, R. Tivey, Assessment and selection of materials for ITER in-vessel components, J. Nucl. Mater. 283 (2000) 10–19.
[11] Y.S. Chen, M.H. Wei, F. Yan, Melting of Cu-Cr-Zr-Mg-RE alloy with high performance, Foundry 6 (2007) 024.
[12] T. Du, Physical-chemical effect of rare earth elements on metallic materials, Acta Metall. Sin. 33 (1997) 69–77.
[13] A. Kisko, J. Talonen, D.A. Porter, L.P. Karjalainen, Effect of Nb microalloying on reversion and grain growth in a High-Mn 204Cu austenitic stainless steel, ISIJ Int. 55 (2015) 2217–2224.
[14] A.K. Shukla, R.S. Kumar, S.V.S.N. Murty, K. Mondal, Enhancement of high temperature ductility of hot-pressed Cu-Cr-Nb alloy by hot rolling, Mater. Sci. Eng. A 577 (2013) 36–42.
[15] Y. Zhang, H.L. Sun, A.A. Volinsky, B.H. Tian, K.X. Song, Z. Chai, P. Liu, Dynamic recrystallization behavior and processing map of the Cu-Cr-Zr-Nd alloy, SpringerPlus 5 (2016) 666.
[16] A. Hernández-Pérez, M. Eddahbi, M.A. Monge, A. Muñoz, B. Savoini, Microstructure and mechanical properties of an ITER-grade Cu-Cr-Zr alloy processed by equal channel angular pressing, Fusion Eng. Des. 98 (2015) 1978–1981.
[17] H. Salavati, Y. Alizadeh, F. Berto, Application the mechanism-based strain gradient plasticity theory to model the hot deformation behavior of functionally graded steels, Struct. Eng. Mech. 51 (2014) 627–641.
[18] N. Srinivasan, Y.V.R.K. Prasad, P.R. Rao, Hot deformation behaviour of Mg-3Al alloy-A study using processing map, Mater. Sci. Eng. A 476 (2008) 146–156.
[19] E. Cerri, E. Evangelista, H.J. McQueen, Overview of the high temperature substructure development in Al-Mg alloys, High. Temp. Mat. Pr-isr. 18 (1999) 227–240.
[20] S. Venugopal, P. Venugopal, S.L. Mannan, Optimisation of cold and worm workability of commercially pure titanium using dynamic materials model(DMM) instability maps, J. Mater. Pr-isr. Tech. 202 (2008) 201.
[21] Y.V.R.K. Prasad, T. Seshacharyulu, Modelling of hot deformation for microstructural control, Int. Mater. Rev. 43 (1998) 243–258.
[22] Z.W. Cai, F.X. Chen, F.J. Ma, J.Q. Guo, Dynamic recrystallization behavior and hot workability of AZ41M magnesium alloy during hot deformation, J. Alloys Comp. 670 (2016) 55–63.
[23] Y.C. Lin, F.Q. Nong, X.M. Chen, D.D. Chen, M.S. Chen, Microstructural evolution and constitutive models to predict hot deformation behaviors of a nickel-based superalloy, Vacuum 137 (2017) 104–114.
[24] Y. Cheng, H. Du, Y. Wei, L. Hou, B. Liu, Metadynamic recrystallization behavior and workability characteristics of HR3C austenitic heat-resistant stainless steel with processing map, J. Mater. Process. Tech. 235 (2016) 134–142.
[25] A. Dehghan-Manshadi, M.R. Barnett, P.D. Hodgson, Recrystallization in AISI 304 austenitic stainless steel during and after hot deformation, Mater. Sci. Eng. A 485 (2008) 664–672.
[26] Y. Nakao, K. Shinozaki, T. Ogawa, H. Sakurai, Effects of Cr and S on ductility-dip cracking susceptibilities in the reheated weld metals of Ni-Cr-Fe ternary alloys: study on microcracks in multipass weld metals of Ni-base alloys (Part 2), Trans. Jpn. Weld. Soc. 24 (1993) 101–106.
[27] J. Li, F.G. Li, J. Cai, R.T. Wang, Z.W. Yuan, F.M. Xue, Flow behavior modeling of the 7050 aluminum alloy at elevated temperatures considering the compensation of strain, Mater. Des. 42 (2012) 369–377.
[28] Y.C. Lin, X.M. Chen, A critical review of experimental results and constitutive descriptions for metals and alloys in hot working, Mater. Des. 32 (2011) 1733–1759.
[29] S.J. Ma, Y. Liu, X.H. Dong, X.P. Zhang, Microstructure and flow stress of Mg-12Gd-3Y-0.5Zr magnesium alloy, J. Wuhan Univ. Technology-Mater. Sci. Ed 28 (2013) 172–177.
[30] C. Zener, J.H. Hollomon, Effect of strain-rate upon the plastic flow of steel, J. Appl. Phys. 15 (1944) 22–27.
[31] C.M. Sellars, W.J. Mctegart, On the mechanism of hot deformation, Acta Metall. 14 (1966) 1136–1138.
[32] S. Yang, D.Q. Yi, H. Zhang, S.J. Yao, Flow stress behavior and processing map of Al-Cu-Mg-Ag alloy during hot compression, J. Wuhan Univ. Technology-Mater. Sci. Ed 23 (2008) 694–698.
[33] C. Zener, J.H. Hollomon, Effect of strain rate upon plastic flow of steel, J. Appl. Phys. 15 (1944) 22–32.
[34] J. Cai, F.G. Li, T.Y. Liu, B. Chen, M. He, Constitutive equations for elevated temperature flow stress of Ti-6Al-4V alloy considering the effect of strain, Mater. Des. 32 (2011) 1144–1151.
[35] D. Samantaray, S. Mandal, A.K. Bhaduri, A comparative study on Johnson Cook, modified Zerilli-Armstrong and Arrhenius-type constitutive models to predict elevated temperature flow behaviour in modified 9Cr-1Mo steel, Comp. Mater. Sci. 47 (2009) 568–576.
[36] C.H. Liao, H.Y. Wu, C.T. Wu, F.J. Zhu, S. Lee, Hot deformation behavior and flow stress modeling of annealed AZ61 Mg alloys, Prog. Nat. Sci-Mater. 24 (2014) 253–265.